

# Anisotropic Core-Shell Swift Heavy Ion Tracks in $\beta$ -Ga<sub>2</sub>O<sub>3</sub>

Huan He,<sup>1</sup> Jiayu Liang,<sup>1</sup> Shaowei He,<sup>1</sup> Yanwen Zhang,<sup>2</sup> Jiahui Zhang,<sup>3</sup> Ziqi Cai,<sup>4</sup> Tan Shi,<sup>1</sup> Hang Zang,<sup>1,\*</sup> Flyura Djurabekova,<sup>5</sup> Chaohui He,<sup>1,†</sup> and Junlei Zhao<sup>6,‡</sup>

<sup>1</sup>*School of Nuclear Science and Technology, Xi'an Jiaotong University, Xi'an, Shaanxi 710049, China*

<sup>2</sup>*Department of Nuclear Physics, China Institute of Atomic Energy, Beijing, 102413, China*

<sup>3</sup>*Materials Science and Environmental Engineering Unit, Tampere University, Tampere, 33720, Finland*

<sup>4</sup>*Institute of Modern Physics, Chinese Academy of Sciences, Lanzhou 730000, China*

<sup>5</sup>*Department of Physics and Helsinki Institute of Physics, University of Helsinki, P.O. Box 43, FI-00014, Finland*

<sup>6</sup>*The Hong Kong Microelectronics Research and Development Institute, Hong Kong, 999077, China*

Swift heavy ion (SHI) irradiation generates nanoscale ion tracks through intense electronic excitation, yet the microscopic mechanisms governing their morphology and phase stability in low-symmetry oxides remain poorly understood. Here, a multiscale atomistic simulation framework is employed to investigate SHI-induced track formation and recovery in monoclinic  $\beta$ -Ga<sub>2</sub>O<sub>3</sub> over a wide range of electronic energy losses ( $S_e$ ) and crystallographic orientations. A sequence of distinct structural responses is identified with increasing  $S_e$ : complete lattice recovery at low  $S_e$ , recrystallization into a metastable  $\gamma$ -Ga<sub>2</sub>O<sub>3</sub> phase at intermediate  $S_e$ , and the formation of core-shell ion tracks at high  $S_e$ , consisting of an amorphous core surrounded by a recrystallized  $\gamma$ -phase shell. Despite the essentially isotropic initial energy deposition, the final ion-track morphology exhibits pronounced crystallographic anisotropy, governed by orientation-dependent recovery dynamics. The superior recrystallization along [010] direction is attributed to its exceptionally high elastic stiffness. Notably, SHI irradiation perpendicular to the (100) plane induces a more severe structural response at low  $S_e$  ( $\leq 10$  keV/nm), however, at higher  $S_e$ , it yields a smaller residual ion track compared with the other orientations. The simulated ion-track sizes show excellent quantitative agreement with available experimental measurements over a broad range of  $S_e$  values. These findings establish a unified atomic-scale picture of core-shell track formation and anisotropic recovery in  $\beta$ -Ga<sub>2</sub>O<sub>3</sub>.

Swift heavy ion (SHI) irradiation, defined as the bombardment of materials with massive ions ( $> 40$  amu) at ultrahigh kinetic energies ( $E_k \geq 1$  MeV/amu), has served as a powerful tool for both probing fundamental radiation damage mechanisms and deliberately tailoring material properties [1–6]. The SHI energy is deposited primarily through electronic energy loss ( $S_e$ ) via intense ionization of the target's electron subsystem and triggers a cascade of physical processes: electron-electron scattering, non-equilibrium electron-lattice coupling, and subsequent lattice heating. Depending on the magnitude of  $S_e$  and the material's properties, this can lead to irreversible lattice transformations, including ion-track formation [6–9], phase transition [10, 11], elemental segregation [2]. The ion tracks produced by SHI are conventionally described as cylindrical damage regions with radial symmetry, reflecting the assumed isotropic dissipation of electronic excitation around the ion trajectory. This description is well supported by track measurements normal to high-symmetry crystal planes [12] and in amorphous matrices [7, 13, 14], where rotational invariance justifies cylindrical track cores and underpins thermal-spike-based models. Whether such radial symmetry remains valid in low-symmetry crystals, however, has only recently been critically examined [12].

The monoclinic  $\beta$ -Ga<sub>2</sub>O<sub>3</sub>, an emerging ultrawide-bandgap semiconductor for power, optical, and radiation-hardened electronics, provides a stringent test of this assumption [15–17]. Over recent years, significant research efforts have been devoted to studying the SHI irradiation response of Ga<sub>2</sub>O<sub>3</sub> [16, 18–21]. However, the majority of experimental work has focused on single event effects and macroscale electrical degradation at the device level [16, 19, 20]. At the material level, several experimental studies [21–23] have provided valuable insights into ion-track formation at high  $S_e$ . However, the atomistic mechanisms elucidated by atomic-scale computational modeling remain rather limited due to the lack of suitable interatomic potentials (IAPs).

Recently, molecular dynamics (MD) simulations driven by machine-learned (ML) IAPs, have also been effectively used to investigate keV-range, low- $S_e$  ion-irradiation-induced phase transformations in complex Ga<sub>2</sub>O<sub>3</sub> system [24], serving as an essential complement to experimental studies [10, 25–27]. However, the underlying mechanisms in these cases are governed almost exclusively by nuclear stopping power ( $S_n$ ), resulting in ballistic collision cascades where atoms are displaced through direct binary knock-on events. Therefore, it remains unclear whether comparable structural transitions can be activated under high- $S_e$  SHI irradiation, where primary damage is introduced via ultrafast electronic excitation, columnar thermal spikes, and subsequent lattice destabilization.

In this work, we present a multiscale computational

\* zanghang@xjtu.edu.cn

† hechaohui@xjtu.edu.cn

‡ junlei.zhao@mrdi.org.hk

modeling of SHI-induced track formation in  $\beta$ -Ga<sub>2</sub>O<sub>3</sub>, combining electronic energy deposition with ML-MD simulations to capture the full evolution from initial excitation to permanent structural modification (see Supplementary Information Fig. S1). By systematically mapping crystallographic orientations and  $S_e$ , we demonstrate that ion-track formation in this low-symmetry monoclinic oxide is intrinsically anisotropic, challenging the conventional assumption of radial symmetry and revealing orientation-dependent thresholds, morphologies, and recovery kinetics.

## RESULTS

The multiscale simulation of SHI irradiation begins with the Monte Carlo (MC) modeling of the initial ionization processes. Geant4 software [28] was utilized to simulate the resulting spatial distribution of electron excitations within the  $\beta$ -Ga<sub>2</sub>O<sub>3</sub> target. The type and energy of incident ions are determined firstly to cover a wide range of  $S_e$ . Four representative types of ions and the corresponding  $S_e$  are simulated in this work, as listed in Table I. It is worth noting that the simulated O, Kr and Ta ions aligns with previous experimental studies on SHI irradiation of  $\beta$ -Ga<sub>2</sub>O<sub>3</sub>.

Table I. Details of SHI irradiation ion types, ion energies, and corresponding calculated  $S_e$  values.

Ion type	Ion energy (MeV)	$S_e$ (keV/nm)
O [23]	12.0	3.02
Xe	19.6	10.00
Kr [22]	460	18.23
Ta [22]	1179	43.87

Following the MC calculations of SHI irradiation, the electronic energy deposition data was applied in a numerical two-temperature model (TTM). Within the TTM framework, the electron and lattice subsystems are treated as two coupled heat baths. The spatiotemporal evolution of the lattice energy under  $S_e$  of 10 keV/nm and 44 keV/nm are presented in Figure 1a and b, respectively. In both cases, the lattice-energy profiles exhibit an initial sharp rise followed by a slower decay and spatial broadening. This behavior reflects the rapid transfer of energy from the excited electronic subsystem to the lattice and its subsequent redistribution via thermal diffusion. Shortly after the peak energy deposition, the electron and lattice subsystems approach local thermal equilibrium ( $T_e \approx T_l$ ), resulting in a Gaussian-like spatial distribution of the deposited lattice kinetic energy. The resulting energy distributions further indicate that the total deposited lattice energy increases monotonically with increasing electronic energy loss. Higher  $S_e$  values produce larger lattice-energy peaks and more extended high-energy regions, implying stronger local atomic displace-

ments and an increased likelihood of thermally driven defect formation.

Owing to the intrinsic limitations of the TTM in describing atomic-scale structural dynamics, the lattice energy deposition profiles obtained from TTM simulations are coupled to MD simulations lastly, establishing a multiscale framework to probe the atomic-level response of Ga<sub>2</sub>O<sub>3</sub> under SHI irradiation. All MD simulations were conducted by LAMMPS software [29] under 300 K and the fast ML-IAP of tabGAP [24, 30] were used in this work. Here SHI irradiation perpendicular to (100) direction is presented firstly as an example. For the lower  $S_e$  of 10 keV/nm, the simulated cross-sections of atomic displacement is presented in Fig. 1c. Only a small and highly localized region of atomic displacement is formed at approximately 11 ps after ion impact. As the displaced atoms dissipate their residual kinetic energy, a transient lattice disorder emerges around 30 ps, producing a short-lived amorphous pocket with a radius of roughly 1.5 nm. However, due to the limited energy deposition, this amorphous zone subsequently undergoes rapid structural recovery. By the end of the simulation (301 ps), no stable amorphous domains persist, confirming that the deposited energy is insufficient to form a stable ion track or to induce permanent amorphization in  $\beta$ -Ga<sub>2</sub>O<sub>3</sub>.

In contrast, for the high  $S_e$  of 44 keV/nm shown in Fig. 1d, an extensive and severe disordering process is initiated, progressing through several distinct stages. A significant atomic displacement is already evident at 6 ps after SHI impact due to the substantially larger kinetic energy imparted to the lattice. Subsequently, this initial damage zone expands radially, reaching a lateral extent of approximately 7 nm by 31 ps. Such dynamic disordering is characteristic of ion-induced amorphization, and the central region of the ion track evolves into a fully amorphous structure where the energy deposition density is highest. Notably, this amorphization process is transient. After approximately 40 ps, the tendency toward amorphization is markedly suppressed and gives way to a recrystallization process that dominates the subsequent structural evolution. As illustrated by the time-sequential atomic configurations in Fig. 1(h), lattice fringes reappear in the peripheral region of the track (region 3), indicating the nucleation and growth of recrystallized domains. Ultimately, although a large fraction of atoms return to their original crystalline positions, a residual disordered core (region 2) with a radius of 4.8 nm persists at the track center.

With respect to the other electronic energy losses, an analogous structural evolution is observed, as shown in Supplementary Information Fig. S2. Under the very low  $S_e$  of 3 keV/nm, corresponding to irradiation by O ions, the overall crystal structure remains essentially intact, exhibiting negligible disruption after SHI irradiation. Only minor lattice vibrations and local bond-angle fluctuations occur. This observation is consistent with recent experimental finding that no detectable ion tracks form in  $\beta$ -Ga<sub>2</sub>O<sub>3</sub> under 12 MeV O ion irradiation.

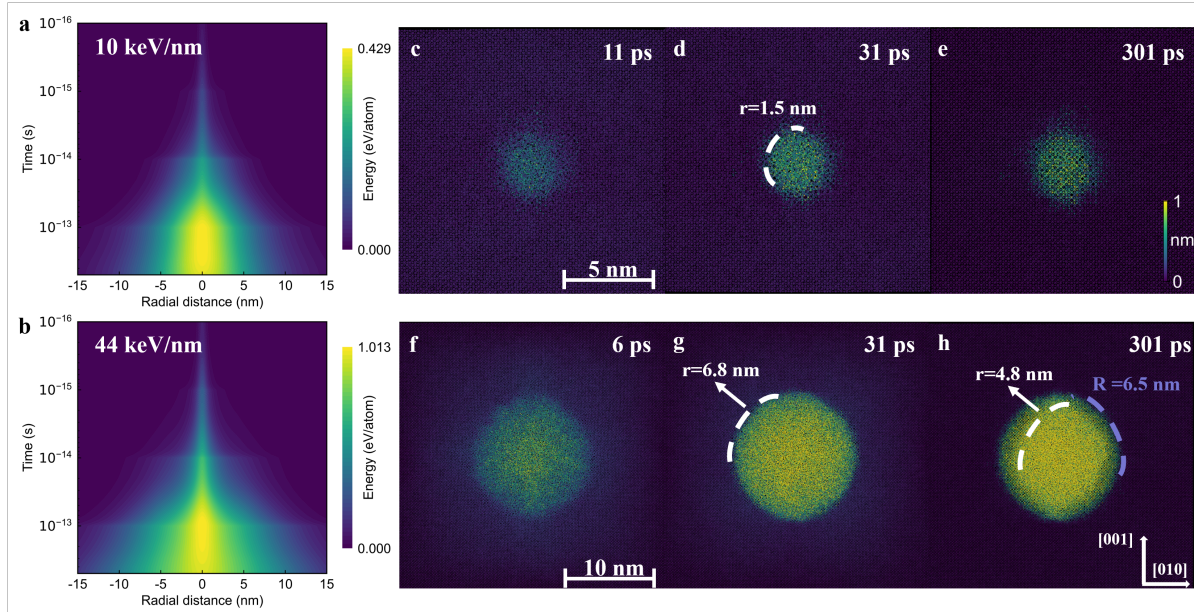
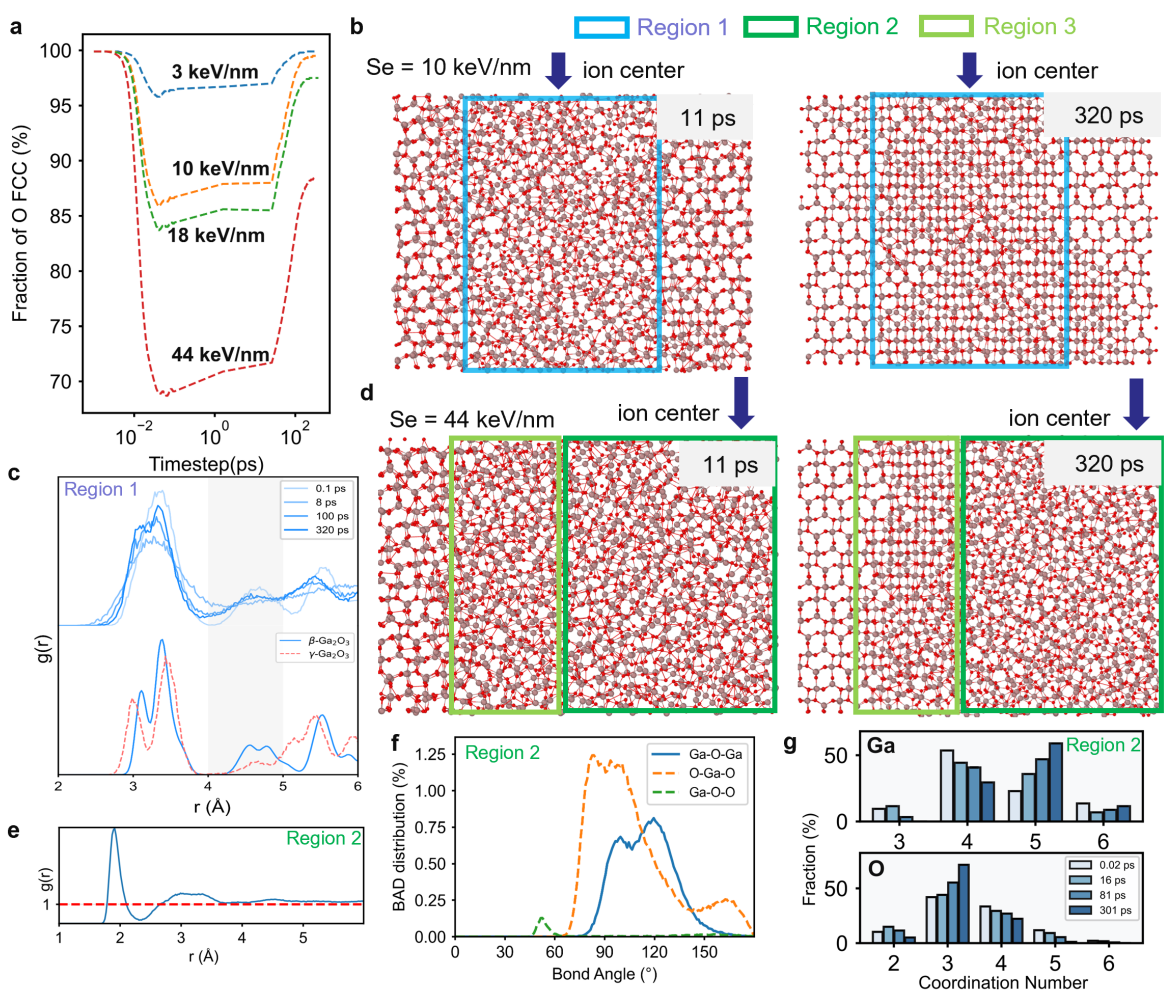


Figure 1. **Spatiotemporal lattice-energy evolution and ion-track morphology under low and high  $S_e$ .** **a,b** Spatiotemporal profiles of lattice energy obtained from TTM simulations at  $S_e$  of 10 keV/nm and 44 keV/nm, respectively. **c-h** Cross-sectional morphologies from MD simulations with  $S_e = 10$  keV/nm and 44 keV/nm, colored by atomic displacement magnitude. All images correspond to the central cross section of the simulated region, representing an effective sample thickness of 5 nm. The view direction is normal to the (100) plane.

ation [23]. Wigner-Seitz defect analysis also confirms that no stable defects are generated under this condition. For intermediate  $S_e$  of 18 keV/nm, the enhanced electronic energy deposition results in the formation of a transient amorphous region with an initial radius of approximately 6–8 nm immediately after SHI impact. In contrast to the more persistent amorphous regions produced at 44 keV/nm, the amorphous zone formed in this intermediate  $S_e$  regime exhibits partial recrystallization within 15–20 ps. The spatial extent of the amorphous region becomes nearly equal to that of the recrystallized area. This suggests that the competition between defect generation and thermal recovery reaches an approximate equilibrium under this excitation condition.

To elucidate the damage mechanism of  $\beta$ -Ga<sub>2</sub>O<sub>3</sub> under SHI irradiation, we performed a detailed structural analysis focusing on the whole evolution process. Although Ga and O occupy multiple nonequivalent Wyckoff sites, the O sublattice preserves a face-centered-cubic (FCC) topology that serves as a robust order parameter for tracking crystalline recovery [26]. As shown in Fig. 2a, the FCC fraction of O sublattice exhibits a universal two-stage behavior across all  $S_e$  values. A rapid disordering within 0.1 ps, followed by gradual recovery extending to tens or even hundreds of picoseconds. At low  $S_e$  (3 keV/nm), the transient disordering is mild, and the O sublattice eventually returns to its pristine FCC arrangement. No residual damage is detected, consistent with experimental reports showing the absence of ion tracks in  $\beta$ -Ga<sub>2</sub>O<sub>3</sub> irradiated with low- $S_e$  ions [23].

At intermediate  $S_e$  of 10 keV/nm, the O sublattice largely restores its FCC-like order, whereas the Ga sublattice exhibits only partial structural recovery. As shown in Fig. 2b, the atomic configuration undergoes substantial rearrangement during the rapid thermal quench, but residual disorder remains primarily associated with Ga sites. Wigner-Seitz defect analysis further indicates that only  $\sim 2\%$  of atoms form persistent defects while these defects are overwhelmingly Ga vacancies ( $\sim 98.5\%$ ). Among them, Ga<sub>2</sub>-site vacancies constitute 57.7% of all Ga vacancies, consistent with the lower displacement energies characteristic of Ga<sub>2</sub> atoms [30]. This asymmetric recovery between the O and Ga sublattices drives the system into nonequilibrium reconstruction pathways, yielding a metastable  $\gamma$ -like configuration rather than restoring the pristine  $\beta$ -phase. This behavior is also clearly reflected in the Ga-Ga pair radial distribution functions (RDFs) in the core region. As shown in Fig. 2c, the RDF at 8 ps exhibits a broad and featureless profile characteristic of a fully amorphous state. By 320 ps, the RDF sharpens markedly, indicating substantial recrystallization; however, the resulting peak positions and relative intensities do not match those of monoclinic  $\beta$ -Ga<sub>2</sub>O<sub>3</sub>. In particular, the absence of the characteristic 4–5 Å peak of the second Ga-Ga shell confirms that the recovered structure does not revert to its original  $\beta$  lattice. Instead, the RDF features are consistent with a metastable  $\gamma$ -like configuration, resembling structural transformations previously observed under high-dose, low-energy irradiation dominated by nuclear stopping [26]. In contrast, the



**Figure 2. Structural analysis of  $\beta$ - $\text{Ga}_2\text{O}_3$  under SHI irradiation perpendicular to (100) direction at different electronic energy losses.** **a** O FCC order parameter evolution at different  $S_e$  values. **b** Atomic configurations at 30 ps and 320 ps ( $S_e = 10 \text{ keV/nm}$ ). Red (blue) atoms are Ga (O) atoms. **c** Evolution of Ga–Ga RDF of the track core (region 1,  $r \leq 2.5 \text{ nm}$ ). **d** Atomic configurations at 30 ps and 320 ps ( $S_e = 44 \text{ keV/nm}$ ). **e** The overall RDF of the track core (Region 2,  $r \leq 4.5 \text{ nm}$ ). **f** Bond-angle distribution (BAD) of Region 2 at 320 ps. **g** Coordination-number distributions of Region 2.

present transition arises solely from electronic energy deposition, demonstrating that electronic excitation alone is also sufficient to induce and stabilize this  $\gamma$ -like phase. The resulting  $\gamma$ -phase interface remains stable throughout the simulation, highlighting its robust metastable persistence.

In the high- $S_e$  regime, the system exhibits a qualitatively different structural response. At the highest  $S_e$  of 44 keV/nm, the ion track no longer remains structurally uniform but instead displays pronounced radial heterogeneity. Based on the local structural characteristics, the track can be divided into three distinct radial regions: a central core ( $r \leq 4.5 \text{ nm}$ , Region 2 in Fig. 2d), an intermediate shell (Region 3), and the surrounding crystalline matrix, forming a three-phase core-shell morphology, as illustrated in Fig. 2d. To identify the structural nature of the track core, we examine the RDF and bond-angle distribution (BAD) of Region 2. As shown in Fig. 2e,

the total RDF rapidly converges to unity beyond the first-neighbor shell, indicating the absence of long-range order. The BAD further reveals broad distributions of Ga–O–Ga and O–Ga–O triplet angles spanning from 60° to 130°. In particular, the O–Ga–O angles exhibit characteristic peaks near 83°, 94°, and 163°, while Ga–O–Ga angles preferentially occur around 100° and 120°. These angular features closely resemble those of amorphous structures obtained from direct annealing simulations [31], confirming the amorphous nature of the track core. In addition, Ga–O–O triplets with a characteristic angle near 52° are identified, providing a structural origin for the small peak previously reported in Ref. [24].

The structural evolution of the amorphous core is further quantified by the coordination-number distributions of Ga and O atoms, as shown in Fig. 2g. In the pristine crystal, Ga atoms predominantly exhibit fourfold coordination with an approximately 1:1 ratio.

Upon SHI irradiation, the fraction of sixfold Ga atoms decreases sharply from  $\sim 50\%$  to  $\sim 10\%$  within the first 0.1 ps and remains at this low level thereafter. Meanwhile, the population of fourfold Ga atoms initially increases, reflecting a rapid reduction in coordination. As the system evolves, these fourfold Ga atoms progressively transform into fivefold configurations, which ultimately dominate the amorphous core, reaching nearly 60% in the final state. Throughout the first 80 ps, a small fraction ( $\sim 10\%$ ) of threefold Ga atoms is observed, but this coordination state is transient and disappears in the final configuration. Overall, the Ga coordination evolution indicates a sequential transformation from sixfold to fourfold and finally to fivefold states, consistent with the preferential displacement of Ga<sub>2</sub> atoms reported in threshold displacement energy calculations [30]. In contrast, the oxygen sublattice exhibits a distinct coordination evolution. Initially, threefold and fourfold O atoms are present in an approximate 2:1 ratio. Both populations decrease rapidly within the first 0.1 ps after irradiation, giving rise to twofold and fivefold states. As the amorphous structure stabilizes, the fraction of threefold O atoms increases steadily, ultimately reaching 71.5% in the final state, while the population of fourfold O stabilizes at approximately 22%. Higher coordination states remain rare, with only  $\sim 5\%$  of O atoms being twofold and fewer than 1% exhibiting fivefold or sixfold. These results indicate that, despite substantial disordering, the O sublattice within the ion-track core retains a predominantly low-coordination character.

In addition, the RDF of final intermediate shell (Region 3) closely resemble those observed in the track core formed at a lower  $S_e$  of 10 keV/nm (Region 1). Accordingly, the ion track induced by the highest  $S_e$  can be inferred to consist of three structurally distinct forms of Ga<sub>2</sub>O<sub>3</sub>: an amorphous core (Region 2), a  $\gamma$ -phase shell (Region 3), and the surrounding pristine  $\beta$  matrix.

Building on the above analysis of local structural responses, we next examine how these atomic-scale transformations manifest at the mesoscale in the form of ion-track morphology. Figure 3 shows the final-state oxygen lattice-order maps for SHI irradiation perpendicular to the (100) plane at increasing electronic energy loss  $S_e$ . A clear sequence of distinct structural responses is identified as  $S_e$  increases. At low  $S_e$  (3 keV/nm), the transient lattice disorder induced by electronic excitation fully recovers, leaving the crystalline framework essentially intact. At intermediate  $S_e$  (10 keV/nm), partial melting followed by recrystallization gives rise to a metastable  $\gamma$ -Ga<sub>2</sub>O<sub>3</sub> phase within the irradiated region. At high  $S_e$  (18 keV/nm and 44 keV/nm), a well-defined core-shell ion-track morphology emerges, consisting of a highly disordered or amorphous core surrounded by a recrystallized shell dominated by the  $\gamma$  phase. This progression underscores the strong dependence of SHI-induced structural evolution on the deposited electronic energy density. Notably, the spatial distribution of FCC O atoms becomes strongly anisotropic at the highest  $S_e$ , suggesting that

the resulting ion-track morphology is highly sensitive to crystallographic orientation. To move beyond qualitative visualization, we employ the local configurational entropy [32, 33] as a mesoscale structural descriptor to quantitatively compare ion-track morphologies formed under SHI irradiation, also perpendicular to four representative crystallographic planes, (100), (010), (001), and (201) of  $\beta$ -Ga<sub>2</sub>O<sub>3</sub>.

Figure 4a-d presents the ion track morphology at the highest  $S_e$  of 44 keV/nm. A pronounced dependence of the ion-track morphology on the irradiation direction is evident. For SHI irradiation perpendicular to (100) plane, the track cross section exhibits an elongated elliptical, or nearly rhombic shape. In contrast, irradiation perpendicular to (010) plane results in a distinctly asymmetric track profile, reflecting the strongly anisotropic atomic arrangement within the (010) plane. A comparable elliptical morphology is obtained for SHI irradiation perpendicular to (001) direction. Remarkably, when viewed the SHI irradiation perpendicular to the (201) plane, the ion track adopts a quasi-hexagonal geometry, indicating enhanced structural coherence associated with this crystallographic orientation.

Due to the pronounced anisotropy of  $\beta$ -Ga<sub>2</sub>O<sub>3</sub>, a unique determination of the ion-track size from atomistic configurations alone is nontrivial. We therefore analyze one-dimensional profiles of the configurational entropy,  $\Omega$ , along the lateral principal axes passing through the track center, as shown in Figure 4e-h. Despite the strong projection-dependent track shapes, all profiles exhibit a common entropy topology:  $\Omega \approx -4$  in the crystalline matrix, a sharp increase at intermediate distances (5.0–7.5 nm) corresponding to a structurally transformed shell associated with a transient  $\gamma$  phase, and a central plateau with  $\Omega \in [-2.5, -2.0]$  defining the fully amorphous track core. This universal entropy further demonstrates that ion tracks in  $\beta$ -Ga<sub>2</sub>O<sub>3</sub> prefer the multilayer core-shell structure, independent of crystallographic orientation.

Based on the entropy-based criterion, the size of ion-track and recovered  $\gamma$  phase are summarized in Table II. Local structural entropy of other  $S_e$  are displayed in Supplementary Information Figs. S3 and S4. Though a pronounced crystallographic anisotropy is observed in the final ion-track morphology, the combined size of the amorphous core and the surrounding  $\gamma$ -phase region remains nearly constant for all crystallographic orientations, with characteristic radii of approximately 7.5 and 15 nm at 18 keV/nm and 44 keV/nm, respectively. This invariance demonstrates that the initial radial distribution of electronic energy deposition and the ensuing amorphization process are largely isotropic. Consequently, the pronounced anisotropy in the final amorphous core size must originate predominantly from orientation-dependent post-irradiation recovery processes rather than from the primary damage stage.

Irrespective of the irradiation direction, the final amorphous core is consistently more confined along the [010]

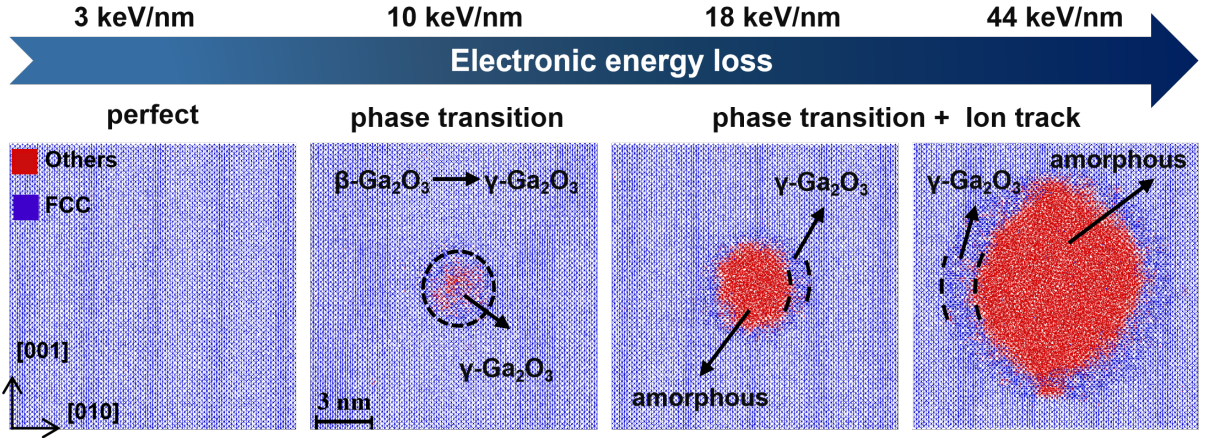


Figure 3. Final state of oxygen lattice order mapping under different SHI irradiation perpendicular to (100) plane.

direction. In particular, for SHI irradiation perpendicular to the (100) and (001) planes, recovery along [010] is significantly more efficient than along other directions, resulting in the flattened elliptical track morphologies shown in Figure 4a and c. This anisotropic recovery behavior is in excellent agreement with the experimental observations of Tracy *et al.* [21], who reported negligible lattice swelling along [010], in contrast to pronounced expansion along [100] and [001]. More broadly, recent studies [12] have demonstrated that the anisotropy of ion-track radii is primarily governed by the elastic properties of material. For highly anisotropic elastic tensor of  $\beta$ -Ga<sub>2</sub>O<sub>3</sub>, our MD simulations also reveal an exceptionally large Young's modulus along the [010] direction, which is approximately 284 GPa (see Supplementary Information Fig. S5). The enhanced stiffness along [010] promotes more efficient stress relaxation for the atomic rearrangement, facilitating recrystallization and effectively suppressing ion-track expansion along this direction. Consequently, these results demonstrate a direct link between elastic anisotropy and anisotropic ion-track recovery in  $\beta$ -Ga<sub>2</sub>O<sub>3</sub>, establishing direction-dependent elastic stiffness as a key intrinsic factor governing ion-track morphology in low-symmetry oxides.

With respect to the ion-track size, the residual ion-track size increases systematically as the  $S_e$  increases. At  $S_e$  of 18 keV/nm, the simulated ion-track diameters remain limited to 2–4.2 nm, accompanied by a high recovery ratio approaching  $\sim$ 47% to 75%. In contrast, at higher  $S_e$  (44 keV/nm), the recovery efficiency drops to 26%–44%, resulting in a pronounced expansion of the amorphous core to diameters of 8.55–11.61 nm. The residual ion-track size of (100) plane remains comparatively smaller than that of other orientations at 18 keV/nm and 44 keV/nm. This behavior reflects a superior recrystallization capability of the (100) orientation under intense SHI irradiation. In contrast, the (201) plane, characterized by a significantly reduced recovery efficiency, accumulates more severe residual dam-

age and develops larger amorphous cores under comparable irradiation conditions. Additionally, the simulated ion-track diameters for the (100) orientation are in quantitative agreement with available experimental measurements over a comparable range of electronic energy losses. At highest  $S_e$  (44 keV/nm), our simulations yield a track diameter of 8.55 nm and 11.61 nm, which is consistent with the value of  $7.8 \pm 0.9$  nm reported by Ai *et al.* [22] at 41 keV/nm and  $8.3 \pm 0.4$  nm measured by Tracy *et al.* [21] for 946 MeV Au-ion irradiation ( $S_e \simeq 45$  keV/nm). At a lower  $S_e$  of 18.3 keV/nm, Ai *et al.* observed a significantly reduced track diameter of  $2.2 \pm 0.4$  nm, which is likewise consistent with the pronounced shrinkage of the track core obtained in our simulations (1.97 nm and 3.12 nm). This level of agreement across different  $S_e$  regimes confirms that the present simulations reliably capture both the characteristic length scale of ion-track formation and the orientation-dependent recovery behavior in  $\beta$ -Ga<sub>2</sub>O<sub>3</sub>.

In contrast to the high  $S_e$  regime, the radiation response at low electronic stopping power ( $S_e = 10$  keV/nm) is governed by a fundamentally different mechanism. As summarized in Table II and Supplementary Figs. S3 and S4, only the (100) plane exhibits a detectable recovered  $\gamma$  phase, whereas the other orientations display merely sparse point defects. This indicates that the (100) plane is intrinsically more susceptible to SHI irradiation under low- $S_e$  conditions. To elucidate this different response, we quantified the fraction of atoms with kinetic energy exceeding 0.5 eV before the atomic response. Although an identical lattice energy profile was imposed for all orientations, the (100) plane consistently exhibits the highest fraction of high  $E_k$  atoms (see Table SX). We attribute it to the significant difference of atomic planar density. The atomic planar density of (100) plane is  $\sim 0.28$  atom/ $\text{\AA}^2$ , which is significantly higher than those of the (010), (001), and (201) planes (approximately 0.13, 0.14, and 0.25 atom/ $\text{\AA}^2$ , respectively). Therefore, more atoms, accounting for the

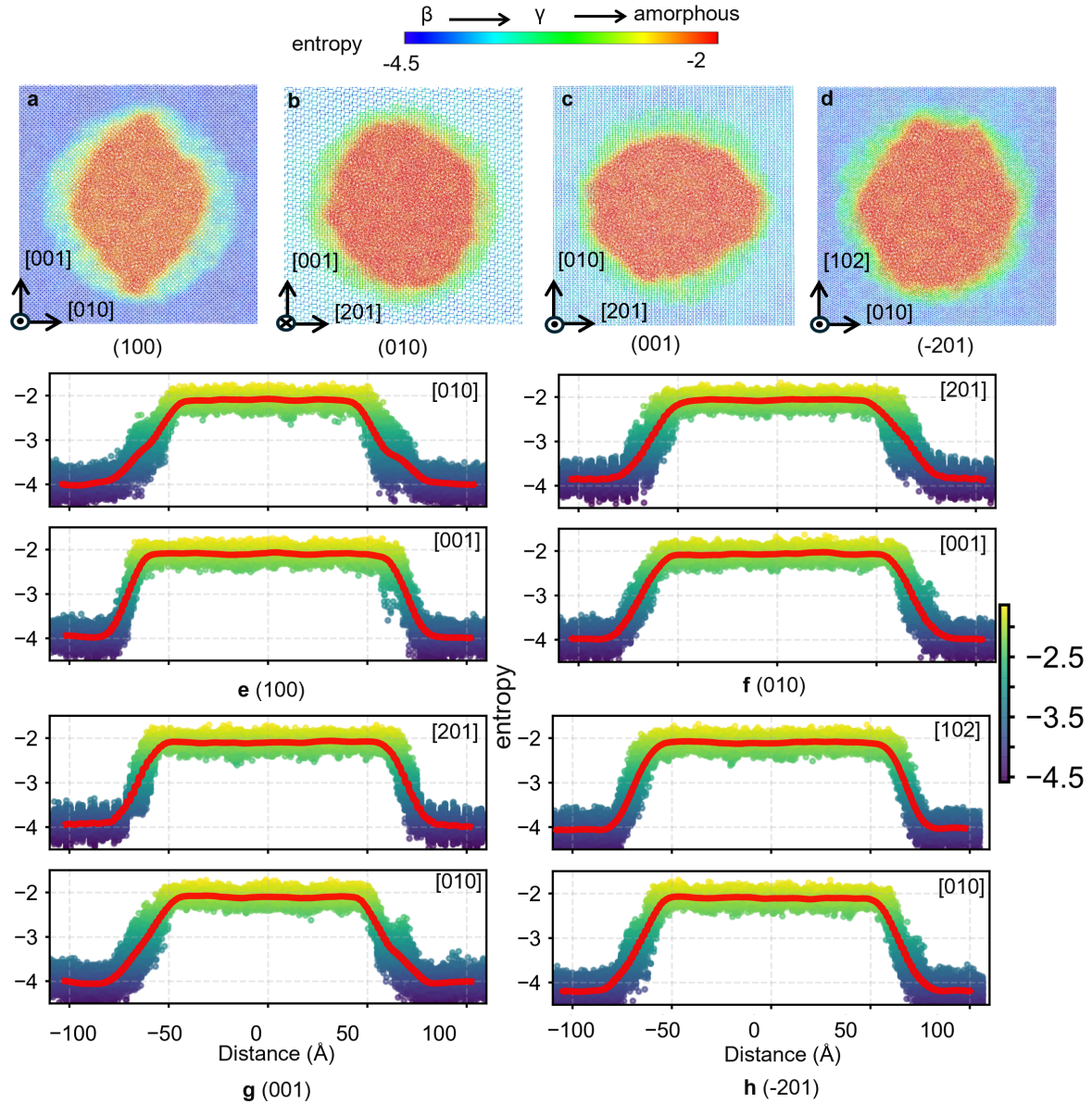


**Figure 4. Ion-track morphology characterized by local structural entropy in  $\beta$ - $\text{Ga}_2\text{O}_3$ .** **a–d** Spatial maps of the local structural entropy for ion tracks formed under SHI irradiation perpendicular to the (100), (010), (001), and ( $\bar{2}01$ ) crystallographic planes at  $S_e$  of 44 keV/nm. **e–h** One-dimensional entropy profiles extracted along the lateral principal crystallographic axes, averaged within a 1.5 nm wide slab, as a function of the radial distance from the track center. The red line denotes the mean entropy at each distance. All analyses are performed within a 5 nm thick region centered on the simulation cell.

enhanced radiation response of the (100) plane at low  $S_e$ .

In summary, the entropy-based analysis reveals a clear separation between the primary damage stage and the post-irradiation recovery process in SHI-irradiated  $\beta$ - $\text{Ga}_2\text{O}_3$ . While the initial electronic energy deposition and amorphization are essentially isotropic, the final ion-track morphology is governed by strongly orientation-dependent recovery dynamics. The pronounced confinement of the amorphous core along [010] originates from

the exceptionally high elastic stiffness along this direction, which promotes efficient stress relaxation and recrystallization during the thermal-spike cooling stage. At high energy losses, this recovery anisotropy dictates the residual track size, whereas at low energy losses, the radiation response is controlled by the competition between deposited energy and crystallographic atomic planar density. These findings establish elastic anisotropy as a key factor controlling ion-track recovery in low-symmetry oxides and provide a unified framework for understanding

Table II. Simulated ion-track size,  $\gamma$ -phase sizes, and recovery ratios for different crystallographic planes and principal axes in  $\beta\text{-Ga}_2\text{O}_3$  under SHI irradiation at different electronic energy losses  $S_e$ .

$S_e$ (keV/nm)	Plane	Axis	Track size (nm)	$\gamma$ phase size (nm)	Recovery ratio (%) <sup>a</sup>
10.0	(1 0 0)	-	0	5.42	-
	(0 1 0)	-	-	-	-
	(0 0 1)	-	-	-	-
	( $\bar{2}$ 0 1)	-	-	-	-
18.2	(1 0 0)	[0 1 0]	1.97	5.90	74.97
		[0 0 1]	3.12	4.30	57.95
	(0 1 0)	[2 0 1]	2.97	5.35	64.30
		[0 0 1]	3.67	4.59	55.57
	(0 0 1)	[2 0 1]	4.24	3.86	47.65
		[0 1 0]	3.13	4.88	60.92
	( $\bar{2}$ 0 1)	[1 0 2]	3.68	3.82	50.93
		[0 1 0]	3.83	4.32	53.01
	(1 0 0)	[0 1 0]	8.55	6.62	43.64
		[0 0 1]	11.61	4.17	26.43
43.9	(0 1 0)	[2 0 1]	9.61	6.87	41.69
		[0 0 1]	11.08	4.90	30.66
	(0 0 1)	[2 0 1]	11.07	4.66	29.62
		[0 1 0]	9.18	5.70	38.31
	( $\bar{2}$ 0 1)	[1 0 2]	11.02	4.27	27.93
		[0 1 0]	10.43	4.42	29.76

<sup>a</sup> Recovery ratio defined as  $D_\gamma/(D_{\text{track}} + D_\gamma)$ .

orientation-dependent SHI effects in  $\beta\text{-Ga}_2\text{O}_3$ .

## METHODS

**Monte Carlo Simulation.** The interaction of swift heavy ions with  $\text{Ga}_2\text{O}_3$  was simulated using the Monte Carlo particle transport code Geant4. A rectangular  $\text{Ga}_2\text{O}_3$  target was constructed with a top surface area of  $39.9 \text{ nm} \times 39.9 \text{ nm}$ . Heavy ions were injected vertically along the center of the top surface. The physical processes governing heavy-ion interactions were described using the standard QGSP\_BIC physics list. To enhance the accuracy of low-energy electromagnetic interactions and elastic ion–atom collisions, the G4EmStandardPhysics\_option4 module was additionally incorporated. This combination allows for a reliable description of both ionizing energy loss (electronic stopping) and non-ionizing energy loss (nuclear stopping). The total ionizing energy deposition was accumulated independently in each cell. After simulating a statistically significant number of ion impacts, the average spatial distributions of ionizing energy deposition were obtained.

**Two temperature Model.** The TTM equations were solved numerically by our self-developed TTM code **Femto-2TM**, yielding the spatiotemporal distribution of the energy transferred to the atomic lattice. The target was discretized into a three-dimensional grid of  $101 \times 101 \times 9$  cells within  $39.9 \text{ nm} \times 39.9 \text{ nm} \times 9 \text{ nm}$ . The

numerical equations are given by

$$C_e(T_e) \frac{\partial T_e}{\partial t} = \nabla \cdot [K_e(T_e) \nabla T_e] - g(T_e - T_l) + S_e(\mathbf{r}, t), \quad (1)$$

$$C_l(T_l) \frac{\partial T_l}{\partial t} = \nabla \cdot [K_l \nabla T_l] + g(T_e - T_l). \quad (2)$$

where  $T_e$  and  $T_l$  are the electron and lattice temperatures, respectively.  $C_e$  and  $C_l$  denote the corresponding heat capacities.  $K_e$ ,  $K_l$  are the thermal conductivities and  $g$  is the electron–phonon coupling constant.  $S_e(\mathbf{r}, t)$  represents the electronic energy source term derived from the ionizing energy deposition calculated by MC simulations. Details of the parameter can be found in the supporting information.

**Molecular dynamics simulation.** All MD simulation were employed by LAMMPS software [29]. The energy deposition was modeled by imparting initial kinetic energy from TTM simulation. Supercells on the order of  $150 \times 300 \times 300 \text{ \AA}^3$  containing about 115,2000 atoms, were constructed for SHI radiation perpendicular to the (1 0 0) plane. The simulation system size of other planes are similar. The simulated supercell was first equilibrated in isothermal-isobaric (*NPT*) ensemble at 300 K and 0 bar. Subsequently, the SHI irradiation process was simulated in the microcanonical (*NVE*) ensemble, while a 300 K thermostatted outer layer was applied to act as a heat sink. The Langevin thermostat was applied

to boundary regions parallel to the SHI trajectory with a layer thickness of 5 Å. Periodic boundary conditions were applied in all three dimensions. All MD simulations were conducted by the fast machine-learned tab-GAP potential [24] which has been validated for simulating complex radiation-induced phenomena relevant to this study [26, 30]. A variable time step from 0.01 fs to 1 fs was used and a total of 320 ps is simulated. Three independent runs were performed for each configuration to ensure statistical significance. Structural changes dur-

ing the simulations were characterized using the OVITO software [32].

## DECLARATION OF INTERESTS

The authors declare that they have no financial or personal relationships with individuals or organizations that could potentially influence the work reported in this paper.

---

[1] M. C. Ridgway, R. Giulian, D. J. Sprouster, P. Kluth, L. L. Araujo, D. J. Llewellyn, A. P. Byrne, F. Kremer, P. F. P. Fichtner, G. Rizza, H. Amekura, and M. Toulemonde, Role of thermodynamics in the shape transformation of embedded metal nanoparticles induced by swift heavy-ion irradiation, *Phys. Rev. Lett.* **106**, 095505 (2011).

[2] O. Ochedowski, O. Osmani, M. Schade, B. K. Bussmann, B. Ban-d’Etat, H. Lebius, and M. Schleberger, Graphitic nanostripes in silicon carbide surfaces created by swift heavy ion irradiation, *Nat. Commun.* **5**, 3913 (2014).

[3] Y. Zhang, R. Sachan, O. H. Pakarinen, M. F. Chisholm, P. Liu, H. Xue, and W. J. Weber, Ionization-induced annealing of pre-existing defects in silicon carbide, *Nat. Commun.* **6**, 8049 (2015).

[4] M. Lang, F. Djurabekova, N. Medvedev, M. Toulemonde, and C. Trautmann, Fundamental phenomena and applications of swift heavy ion irradiations, in *Comprehensive Nuclear Materials*, edited by R. J. M. Konings and R. E. Stoller (Elsevier, Oxford, 2020) 2nd ed., pp. 485–516.

[5] N. Medvedev, A. E. Volkov, R. Rymzhanov, F. Akhmetov, S. Gorbunov, R. Voronkov, and P. Babaev, Frontiers, challenges, and solutions in modeling of swift heavy ion effects in materials, *J. Appl. Phys.* **133**, 100701 (2023).

[6] H. Amekura, A. Chettah, K. Narumi, A. Chiba, Y. Hirano, K. Yamada, S. Yamamoto, A. A. Leino, F. Djurabekova, K. Nordlund, N. Ishikawa, N. Okubo, and Y. Saitoh, Latent ion tracks were finally observed in diamond, *Nat. Commun.* **15**, 1786 (2024).

[7] M. C. Ridgway, T. Bierschenk, R. Giulian, B. Afra, M. D. Rodriguez, L. L. Araujo, A. P. Byrne, N. Kirby, O. H. Pakarinen, F. Djurabekova, K. Nordlund, M. Schleberger, O. Osmani, N. Medvedev, B. Rethfeld, and P. Kluth, Tracks and voids in amorphous Ge induced by swift heavy-ion irradiation, *Phys. Rev. Lett.* **110**, 245502 (2013).

[8] M. C. Sequeira, J.-G. Mattei, H. Vazquez, F. Djurabekova, K. Nordlund, I. Monnet, P. Mota-Santiago, P. Kluth, C. Grygiel, S. Zhang, E. Alves, and K. Lorenz, Unravelling the secrets of the resistance of GaN to strongly ionising radiation, *Commun. Phys.* **4**, 51 (2021).

[9] P. P. Hu, Z. N. Jin, L. J. Xu, S. X. Zhang, P. F. Zhai, J. Zeng, Z. Z. Li, X. Y. Yan, L. Cai, and J. Liu, Latent tracks induced by swift heavy ions in gallium nitride, *Nucl. Instrum. Methods Phys. Res., Sect. B* **568**, 165855 (2025).

[10] A. Abdullaev, J. Garcia Fernandez, C. Nozais, J. O’Connell, R. Tlegenov, K. Sekerbayev, A. Azarov, A. Leino, T. Fernandez Bouvier, J. Zhao, A. Artinez Pena, N. Medvedev, Z. Utlegulov, Ø. Prytz, F. Djurabekova, and A. Kuznetsov, Ions leaving no tracks, arXiv 10.48550/arXiv.2509.07440 (2025), 2509.07440.

[11] A. K. Gupta, E. Zarkadoula, B. L. Musico, J. A. Hachtel, M. A. Roldan, V. R. Paduri, C. Harris, R. Subedi, M. Ziatdinov, S. V. Kalinin, C. Trautmann, V. Kepens, J. Liu, Y. Zhang, W. J. Weber, and R. Sachan, Unveiling swift heavy ion track morphology in Sr-based high-entropy perovskites, *ACS Nano* **null**, null (2025).

[12] J. Wierbik, H. Heimes, C. Notthoff, S. Dutt, T. Alwadi, A. Kiy, P. Mota-Santiago, N. Kirby, and P. Kluth, Anisotropic fine structure of ion tracks in single crystals, *Phys. Rev. B* **113**, 035306 (2026).

[13] P. Kluth, C. S. Schnohr, O. H. Pakarinen, F. Djurabekova, D. J. Sprouster, R. Giulian, M. C. Ridgway, A. P. Byrne, C. Trautmann, D. J. Cookson, K. Nordlund, and M. Toulemonde, Fine structure in swift heavy ion tracks in amorphous SiO<sub>2</sub>, *Phys. Rev. Lett.* **101**, 175503 (2008).

[14] T. Bierschenk, A. A. Leino, W. Wesch, B. Afra, M. D. Rodriguez, F. Djurabekova, L. Keller, O. H. Pakarinen, K. Nordlund, M. C. Ridgway, and P. Kluth, Formation and self-organisation of nano-porosity in swift heavy ion irradiated amorphous Ge, *Acta Mater.* **261**, 119396 (2023).

[15] S. J. Pearton, J. Yang, P. H. Cary, F. Ren, J. H. Kim, M. J. Tadjer, and M. A. Mastro, A review of Ga<sub>2</sub>O<sub>3</sub> materials, processing, and devices, *Appl. Phys. Rev.* **5**, 011301 (2018).

[16] W.-S. Ai, J. Liu, Q. Feng, P.-F. Zhai, P.-P. Hu, J. Zeng, S.-X. Zhang, Z.-Z. Li, L. Liu, X.-Y. Yan, and Y.-M. Sun, Degradation of  $\beta$ -Ga<sub>2</sub>O<sub>3</sub> Schottky barrier diode under swift heavy ion irradiation, *Chin. Phys. B* **30**, 056110 (2021).

[17] S. J. Pearton, F. Ren, A. Y. Polyakov, E. B. Yakimov, L. Chernyak, and A. Haque, Perspective on comparative radiation hardness of Ga<sub>2</sub>O<sub>3</sub> polymorphs, *J. Vac. Sci. Technol. A* **43**, 038501 (2025).

[18] N. Manikanthababu, B. R. Tak, K. Prajna, S. Sarkar, K. Asokan, D. Kanjilal, S. R. Barman, R. Singh, and B. K. Panigrahi, Swift heavy ion irradiation-induced modifications in the electrical and surface properties of  $\beta$ -Ga<sub>2</sub>O<sub>3</sub>, *Appl. Phys. Lett.* **117**, 142105 (2020).

[19] H. Zhu, Y. Tang, A. Zhong, L. Wang, F. Liu, P. Zhao, J. Liu, L. Shu, Z. Wu, and B. Li, Swift heavy ion irradiation-driven energy band engineering and its profound influence on the photoresponse of  $\beta$ -Ga<sub>2</sub>O<sub>3</sub> ultraviolet photodetectors, *Appl. Phys. Lett.* **124**, 153505 (2024).

[20] T. Ma, X. Li, S. Zhong, Y. Feng, Y. Wang, X. Zhang, C. Peng, H. Zhang, Z. Zhang, X. Liang, and Z. Lei, Single-event burnout in  $\beta$ -Ga<sub>2</sub>O<sub>3</sub> Schottky barrier diode induced by heavy ion irradiation, *Appl. Phys. Lett.* **127**, 123501 (2025).

[21] C. L. Tracy, M. Lang, D. Severin, M. Bender, C. Trautmann, and R. C. Ewing, Anisotropic expansion and amorphization of Ga<sub>2</sub>O<sub>3</sub> irradiated with 946 MeV Au ions, *Nucl. Instrum. Methods Phys. Res., Sect. B* **374**, 40 (2016).

[22] W. Ai, L. Xu, S. Nan, P. Zhai, W. Li, Z. Li, P. Hu, J. Zeng, S. Zhang, L. Liu, Y. Sun, and J. Liu, Radiation damage in  $\beta$ -Ga<sub>2</sub>O<sub>3</sub> induced by swift heavy ions, *Jpn. J. Appl. Phys.* **58**, 120914 (2019).

[23] D. Iancu, E. Zarkadoula, V. Leca, A. Hotnog, Y. Zhang, W. J. Weber, and G. Veliša, Intrinsic property of defective  $\beta$ -Ga<sub>2</sub>O<sub>3</sub> to self-heal under ionizing irradiation, *Scr. Mater.* **268**, 116858 (2025).

[24] J. Zhao, J. Byggmästar, H. He, K. Nordlund, F. Djurabekova, and M. Hua, Complex Ga<sub>2</sub>O<sub>3</sub> polymorphs explored by accurate and general-purpose machine-learning interatomic potentials, *npj Comput. Mater.* **9**, 159 (2023).

[25] A. Azarov, J. Fernández, J. Zhao, *et al.*, Universal radiation tolerant semiconductor, *Nature Communications* **14**, 4855 (2023).

[26] J. Zhao, J. G. Fernández, A. Azarov, R. He, Ø. Prytz, K. Nordlund, M. Hua, F. Djurabekova, and A. Kuznetsov, Crystallization instead of amorphization in collision cascades in gallium oxide, *Phys. Rev. Lett.* **134**, 126101 (2025).

[27] A. Azarov, J. G. Fernández, J. Zhao, R. He, J.-H. Park, D.-W. Jeon, Ø. Prytz, F. Djurabekova, and A. Kuznetsov, Phase glides and self-organization of atomically abrupt interfaces out of stochastic disorder in  $\alpha$ -Ga<sub>2</sub>O<sub>3</sub>, *Nat. Commun.* **16**, 3245 (2025).

[28] S. Agostinelli, J. Allison, K. Amako, J. Apostolakis, H. Araujo, P. Arce, M. Asai, D. Axen, S. Banerjee, G. Barrand, F. Behner, L. Bellagamba, J. Boudreau, L. Broglia, A. Brunengo, H. Burkhardt, S. Chauvie, J. Chuma, R. Chytracek, G. Cooperman, G. Cosmo, P. Degtyarenko, A. Dell'Acqua, G. Depaola, D. Dietrich, R. Enami, A. Feliciello, C. Ferguson, H. Fesefeldt, G. Folger, F. Foppiano, A. Forti, S. Garelli, S. Gianni, R. Giannitrapani, D. Gibin, J. J. Gómez Cadenas, I. González, G. Gracia Abril, G. Greeniaus, W. Greiner, V. Grichine, A. Grossheim, S. Guatelli, P. Gumplinger, R. Hamatsu, K. Hashimoto, H. Hasui, A. Heikkinen, A. Howard, V. Ivanchenko, A. Johnson, F. W. Jones, J. Kallenbach, N. Kanaya, M. Kawabata, Y. Kawabata, M. Kawaguti, S. Kelner, P. Kent, A. Kimura, T. Kodama, R. Kokoulin, M. Kossov, H. Kurashige, E. Lamanna, T. Lampén, V. Lara, V. Lefebure, F. Lei, M. Liendl, W. Lockman, F. Longo, S. Magni, M. Maire, E. Medernach, K. Minamimoto, P. Mora de Freitas, Y. Morita, K. Murakami, M. Nagamatu, R. Nartallo, P. Nieminen, T. Nishimura, K. Ohtsubo, M. Okamura, S. O'Neale, Y. Oohata, K. Paech, J. Perl, A. Pfeiffer, M. G. Pia, F. Ranjard, A. Rybin, S. Sadilov, E. Di Salvo, G. Santin, T. Sasaki, N. Savvas, Y. Sawada, S. Scherer, S. Sei, V. Sirotenko, D. Smith, N. Starkov, H. Stoecker, J. Sulkimo, M. Takahata, S. Tanaka, E. Tcherniaev, E. Safai Tehrani, M. Tropeano, P. Truscott, H. Uno, L. Urban, P. Urban, M. Verderi, A. Walkden, W. Wunder, H. Weber, J. P. Wellisch, T. Wenaus, D. C. Williams, D. Wright, T. Yamada, H. Yoshida, and D. Zschiesche, Geant4—a simulation toolkit, *Nucl. Instrum. Methods Phys. Res., Sect. A* **506**, 250 (2003).

[29] A. P. Thompson, H. M. Aktulga, R. Berger, D. S. Bolintineanu, W. M. Brown, P. S. Crozier, P. J. in 't Veld, A. Kohlmeyer, S. G. Moore, T. D. Nguyen, R. Shan, M. J. Stevens, J. Tranchida, C. Trott, and S. J. Plimpton, LAMMPS - a flexible simulation tool for particle-based materials modeling at the atomic, meso, and continuum scales, *Comp. Phys. Comm.* **271**, 108171 (2022).

[30] H. He, J. Zhao, J. Byggmästar, R. He, K. Nordlund, C. He, and F. Djurabekova, Threshold displacement energy map of Frenkel pair generation in  $\beta$ -Ga<sub>2</sub>O<sub>3</sub> from machine-learning-driven molecular dynamics simulations, *Acta Mater.* **276**, 120087 (2024).

[31] J. Zhang, J. Zhao, J. Byggmästar, E. J. Frankberg, and A. Kuronen, Large-scale atomistic study of plasticity in amorphous gallium oxide with ab-initio accuracy, *Sci. Rep.* **15**, 9492 (2025).

[32] A. Stukowski, Visualization and analysis of atomistic simulation data with OVITO—the open visualization tool, *Modell. Simul. Mater. Sci. Eng.* **18**, 015012 (2010).

[33] T. Liu, T. Wang, Z. Li, E. Zhou, J. Zhao, J. Feng, X. Fei, Y. Guo, F. Djurabekova, S. Liu, and Z. Zhang, Anisotropic kinetics of ion-irradiation-induced phase transition in gallium oxide, *arXiv* 10.48550/arXiv.2601.02770 (2026), 2601.02770.